Post-Earthquake Fold Growth Imaged in the Qaidam Basin, China, With Interferometric Synthetic Aperture Radar

Simon Daout, Barry Parsons, Richard Walker

▶ **To cite this version:**

Simon Daout, Barry Parsons, Richard Walker. Post-Earthquake Fold Growth Imaged in the Qaidam Basin, China, With Interferometric Synthetic Aperture Radar. Journal of Geophysical Research : Solid Earth, 2021, 126 (3), pp.1-15. 10.1029/2020JB021241 . hal-04494137

HAL Id: hal-04494137
https://hal.science/hal-04494137v1

Submitted on 10 Mar 2024

HAL is a multi-disciplinary open access archive for the deposit and dissemination of scientific research documents, whether they are published or not. The documents may come from teaching and research institutions in France or abroad, or from public or private research centers.

L'archive ouverte pluridisciplinaire **HAL**, est destinée au dépôt et à la diffusion de documents scientifiques de niveau recherche, publiés ou non, émanant des établissements d'enseignement et de recherche français ou étrangers, des laboratoires publics ou privés.

Distributed under a Creative Commons Attribution 4.0 International License

Check for updates

JGR Solid Earth

RESEARCH ARTICLE
10.1029/2020JB021241

Post-Earthquake Fold Growth Imaged in the Qaidam Basin, China, With Interferometric Synthetic Aperture Radar

Simon Daout[1], **Barry Parsons**[1], **and Richard Walker**[1]

[1]Department of Earth Sciences, COMET, University of Oxford, Oxford, UK

Key Points:

- Sixteen years of post-seismic transient deformations measured with interferometric synthetic aperture radar
- Spatio-temporal changes of post-seismic rates and patterns have been observed
- Anelastic bulk deformation of the medium in response to fault slip

Supporting Information:

- Supporting Information S1

Correspondence to:
S. Daout,
simon.daout@earth.ox.ac.uk

Citation:
Daout, S., Parsons, B., & Walker, R. (2021). Post-earthquake fold growth imaged in the Qaidam basin, China, with Interferometric synthetic aperture radar. *Journal of Geophysical Research: Solid Earth*, *126*, e2020JB021241. https://doi.org/10.1029/2020JB021241

Received 27 OCT 2020
Accepted 20 FEB 2021

© 2021. The Authors.
This is an open access article under the terms of the Creative Commons Attribution License, which permits use, distribution and reproduction in any medium, provided the original work is properly cited.

Abstract Questions regarding the development of folds and their interactions with the seismic faults within thrust systems remain unanswered. However, estimating fault slip and earthquake hazards using surface observations and kinematic models of folding requires an understanding of how the shortening is accommodated during the different phases of the earthquake cycle. Here, we construct 16-years of interferometric synthetic aperture radar time series across the North Qaidam thrust system (NE Tibet), where three Mw 6.3 earthquakes occurred along basement faults underlying shortened folded sediments. The analysis reveals spatio-temporal changes of post-earthquake surface displacement rates and patterns, which continue more than 10 years after the seismic events. The decomposition of the Sentinel-1 ascending and descending line of sight velocities into vertical and shortening post-earthquake components indicates that long-term transient uplift and shortening is in agreement with the deformation that might be expected from kinematic models of folding. Long-term uplift coincides spatially with young anticlines observed in the geomorphology, with steep gradients in the forelimbs, gentle gradients in the back-limbs, an absence of subsidence in the footwalls, and higher gradients along interpreted bedding planes. Long-term shortening is also different from the surface displacements expected for typical time-varying creep on a narrow dislocation interface and shows rates higher than the average convergence across the whole region. These findings provide evidence for anelastic fold buckling during the post-earthquake phase and highlight the contribution of distributed aseismic deformation to the growth of topography.

1. Introduction

Numerous studies have observed that folds grow primarily due to slip on underlying faults and that their surface expressions, such as anticline geometries, can be used directly to infer long-term fault slip rates (e.g., Brandes & Tanner, 2014; Daëron et al., 2007; Dolan & Avouac, 2007; Guilbaud et al., 2017; Shaw, Connors, et al. 2005; Shaw, Plesch, et al., 2002; Suppe, 1983; Ward & Valensise, 1994). However, the importance of fold buckling and distributed strain to the component of shortening and fold growth is not clear (e.g., Ainscoe et al., 2017; Gonzalez-Mieres & Suppe, 2006; Veloza et al., 2015; Yonkee & Weil, 2010). In other words, it is also recognized in the literature that there is not a simple relationship between slip and fold growth (e.g., Bonanno et al., 2017; Huang & Johnson, 2016; Johnson, 2018).

Some studies have used geodetic measurements of coseismic surface displacements to document growth of anticlines (e.g., Belabbès et al., 2009; Nissen et al., 2007; Stein & King, 1984; Tizzani et al., 2013). However, recent satellite-based measurements have highlighted the observation that the surface ground deformation associated with thrust earthquakes often does not match the present-day or Quaternary active geomorphology in extent and that it is unlikely that repeated earthquakes of the same type could reproduce the observed topography (e.g., Ainscoe et al., 2017; Barnhart, Brengman, et al., 2018; Copley, 2014; Elliott, Jolivet, et al., 2016; Mackenzie et al., 2016). In addition, although simplified models are valuable in many ways, modeling shortening and the associated uplift across a fold-and-thrust belt system with one or two elastic dislocations is an arguable simplification of the complicated history and geometry of a thrusting morphology, which may involve several interconnected faults and folds that interact with each other, multiple bends, and anelastic deformation as in the upper plate around the bends (e.g., Daout, Barbot, Peltzer, Doin, et al., 2016; Davis et al., 1983; Medwedeff & Suppe, 1997; Sathiakumar et al., 2020; Tapponnier, Meyer, et al., 1990; Whipple et al., 2016). Some other geodetic observations have recently documented or/and modeled episodic aseismic ground deformations (e.g., Mariniere et al., 2020) or long-periods of after-

21699356, 2021, 3, Downloaded from https://agupubs.onlinelibrary.wiley.com/doi/10.1029/2020JB021241 by Cochrane France, Wiley Online Library on [10/03/2024]. See the Terms and Conditions (https://onlinelibrary.wiley.com/terms-and-conditions) on Wiley Online Library for rules of use; OA articles are governed by the applicable Creative Commons License

slip that correlate with the present-day geomorphology (e.g., Barnhart, Lohman, & Mellors, 2013; Copley, 2014; Daout, Sudhaus, Kausch, et al., 2019; Elliott, Bergman, et al., 2015; Fielding et al., 2004; Mackenzie et al., 2016; Wimpenny et al., 2017; Zhou et al., 2018). These measurements suggest that the permanent deformation in fold-and-thrust belts might be sometimes created by distributed off-fault deformation (i.e., anelastic buckling of the medium), or aseismic slip on secondary faults branching from the main earthquake fault or around it, and which occur during stages of the earthquake cycle other than the seismic event. Despite the likely importance of those phenomena, little is known about the link between seismic slip on the main fault and slip on secondary faults or distributed deformation following a seismic event. To understand how topography is generated by repeated earthquake cycles and/or by other processes, and to constrain the period within the earthquake cycle during which geomorphological structures are formed, it is necessary, therefore, to bridge the discrepancy between simple geodetic models of fault slip and geological models of fold-and-thrust belts, by combining measurements of surface displacements over a long-time period and with realistic structural fold-and-fault geometries.

The North Qaidam thrust (NQT) system is located at the southernmost part of the Qilian Shan-Nan Shan thrust belt and exhibits segmented anticlines striking in a northwest-southeast direction (Figure 1). In this NE part of the Tibetan Plateau, while major strike-slip faults, such as the Kunlun and Haiyuan Faults, have received considerable attention from the tectonic and geodetic communities, data from the thrust systems in the South Qilian Shan are not widely reported, and little is known about the structural geology of the region (e.g., Fang et al., 2007; Guihua et al., 2013; Meyer et al., 1998; Tapponnier, Zhiqin, et al., 2001; Yin, Dang, Wang, et al., 2008; Yin, Dang, Zhang, et al., 2008). According to sparse global navigation satellite system (GNSS) measurements, about 4–6 mm/yr of convergence is accommodated there in an overall N22°E direction (Liang et al., 2013; Wang et al., 2017) (Figure S1). The region is marked by active seismicity with three M_w6.3 events occurring in a 150 km along-strike area between 2003 and 2009 (Figure 1). The 17 April 2003 Delingha earthquake ruptured part of the Zongwulong thrust with a centroid depth, derived from local seismic network, of 16 km (Sun et al., 2012), in a section of the North Qaidam Shan which was previously unrecognized as active (Figure 1b). It was followed by extensive and long-lasting logarithmic post-seismic slip that coincided with the Delingha anticline and continued into 2011 along a north-dipping creeping structure (Daout, Sudhaus, Kausch, et al., 2019). As reported by the authors (Daout, Sudhaus, Kausch, et al., 2019), shallow creep is in agreement with a rate-strengthening fault behavior of the uppermost part of the crust, but the duration, the amplitude, and the spatial extent of the observed surface displacements following the 2003 earthquake, during the 2003–2011 Envisat period, is a notable particularity, despite the low strain rate of the area. The 10 November 2008 and the 28 August 2009 Haixi earthquakes occurred in close proximity to each other within the Olongbulak Shan, to the west of the Delingha rupture (Figure 1), and were followed by a period of an increased rate of seismicity in the region and aseismic slip (Daout, Steinberg, Isken, et al., 2020; Daout, Sudhaus, Kausch, et al., 2019; Elliott, Parsons, et al., 2011; Feng, 2015; Guihua et al., 2013; Liu, Xu, Li, et al., 2016; Liu, Xu, Wen, & Fok, 2015; Liu, Xu, Wen, & Li, 2016). Daout, Steinberg, Isken, et al. (2020) modeled the 2008 earthquake with a ∼32° north-dipping fault that roots under the Olongbulak pop-up structure at ∼12 km depth (top edge of the fault) (Figure 1b), as well as down-dip aferslip along a coplanar north-dipping plane. They also inferred three south-dipping segmented ∼55–75° high-angle faults for the 2009 earthquake with fault tip depths between ∼2.5 and 4.5 km and three post-seismic faults with similar geometries than the three earthquake patches (Daout, Steinberg, Isken, et al., 2020). They, therefore, inferred a low-angle north-dipping décollement that roots at the bottom of the fold-and-thrust belt structures of the NQT transferring the shortening rate from the north, along the Qilian Shan, to the south, in the Qaidam basin, in agreement with the southward expansion of the South Qilian Shan since the Neogene (Pang et al., 2019) (Figure 1b).

In this study, we conduct a Multi-Temporal Interferometric Synthetic Aperture Radar analysis across this northeastern part of the Tibetan Plateau using both C-band Envisat (2003–2011) data derived from Daout, Sudhaus, Kausch, et al. (2019), and C-band Sentinel-1 (2014–2019) data (Figures 1 and S2). We processed the Sentinel-1 data set and corrected both Envisat and Sentinel-1 data sets for tropospheric path delays using the newly ERA-5 atmospheric model provided by the European Center for Medium-Range Weather Forecasts (ECMWF). To capture and quantify the spatio-temporal change of the aseismic strain release that follow the 2003 Delingha (Figure 2) and the 2008–2009 Haixi (Figure 3) earthquakes, we extract linear ground velocities over different time spans with a parametric decomposition. We then decompose both

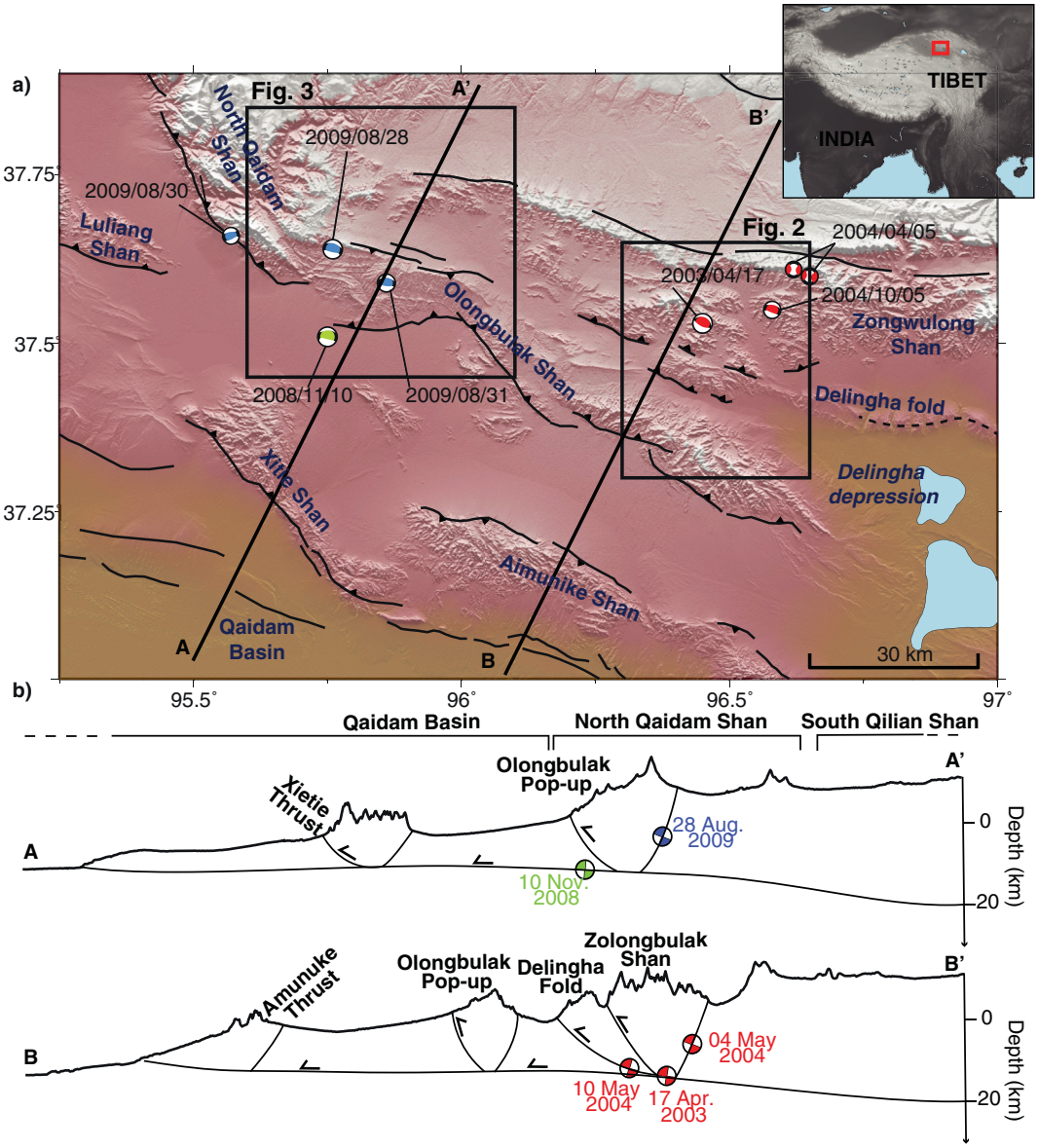

Figure 1. (a) Seismotectonic setting of the northeastern part of the North Qaidam thrust system with fault traces and focal mechanisms of the eight $M_w > 5.2$ events (USGS catalog) that occurred within the Olongbulak and Zongwulong ranges from 2003 to 2009. Topography is from the SRTM 30 m hill-shaded Digital Elevation Model. Top right inset: regional setting and location of the study area (red box). (b) Two topography profiles marked AA' and BB' in (a) with regional conceptual interpreted fault structures and earthquake locations derived from Daout, Sudhaus, Kausch, et al. (2019), Daout, Steinberg, Isken, et al. (2020), and the available cross-sections of Yin, Dang, Wang, et al. (2008), Fang et al. (2007), and Guihua et al. (2013).

ascending and descending line of sight (LOS) velocities into an N22°E horizontal velocity, which is the main direction of shortening, perpendicular to the overall orientation of the North Qaidam thrust systems, and a vertical surface velocity (Figures 4 and 5), to infer two structural models of the folds and associated faults for the two areas.

21699356, 2021, 3, Downloaded from https://agupubs.onlinelibrary.wiley.com/doi/10.1029/2020JB021241 by Cochrane France, Wiley Online Library on [10/03/2024]. See the Terms and Conditions (https://onlinelibrary.wiley.com/terms-and-conditions) on Wiley Online Library for rules of use; OA articles are governed by the applicable Creative Commons License

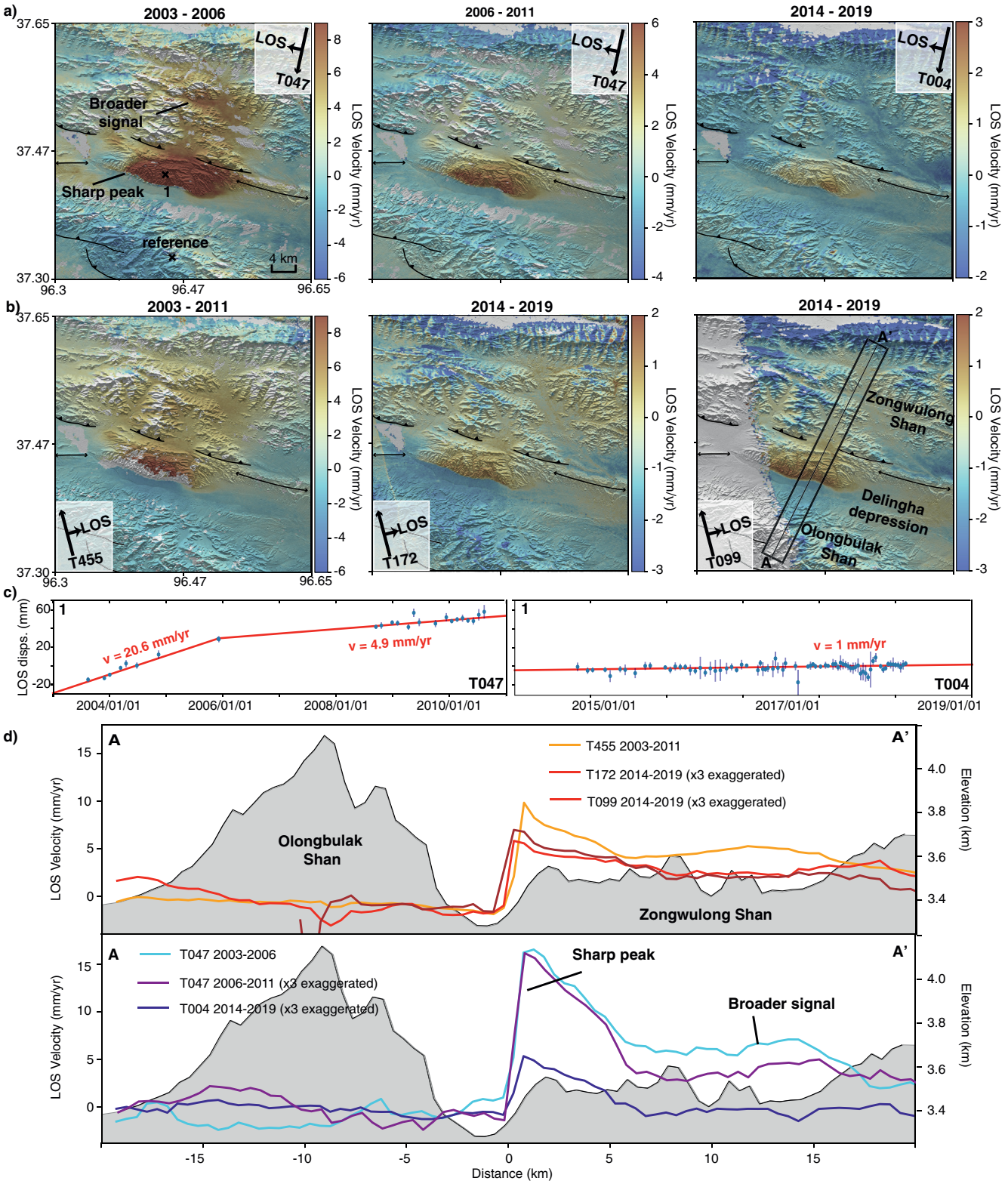

21699356, 2021, 3, Downloaded from https://agupubs.onlinelibrary.wiley.com/doi/10.1029/2020JB021241 by Cochrane France, Wiley Online Library on [10/03/2024]. See the Terms and Conditions (https://onlinelibrary.wiley.com/terms-and-conditions) on Wiley Online Library for rules of use; OA articles are governed by the applicable Creative Commons License

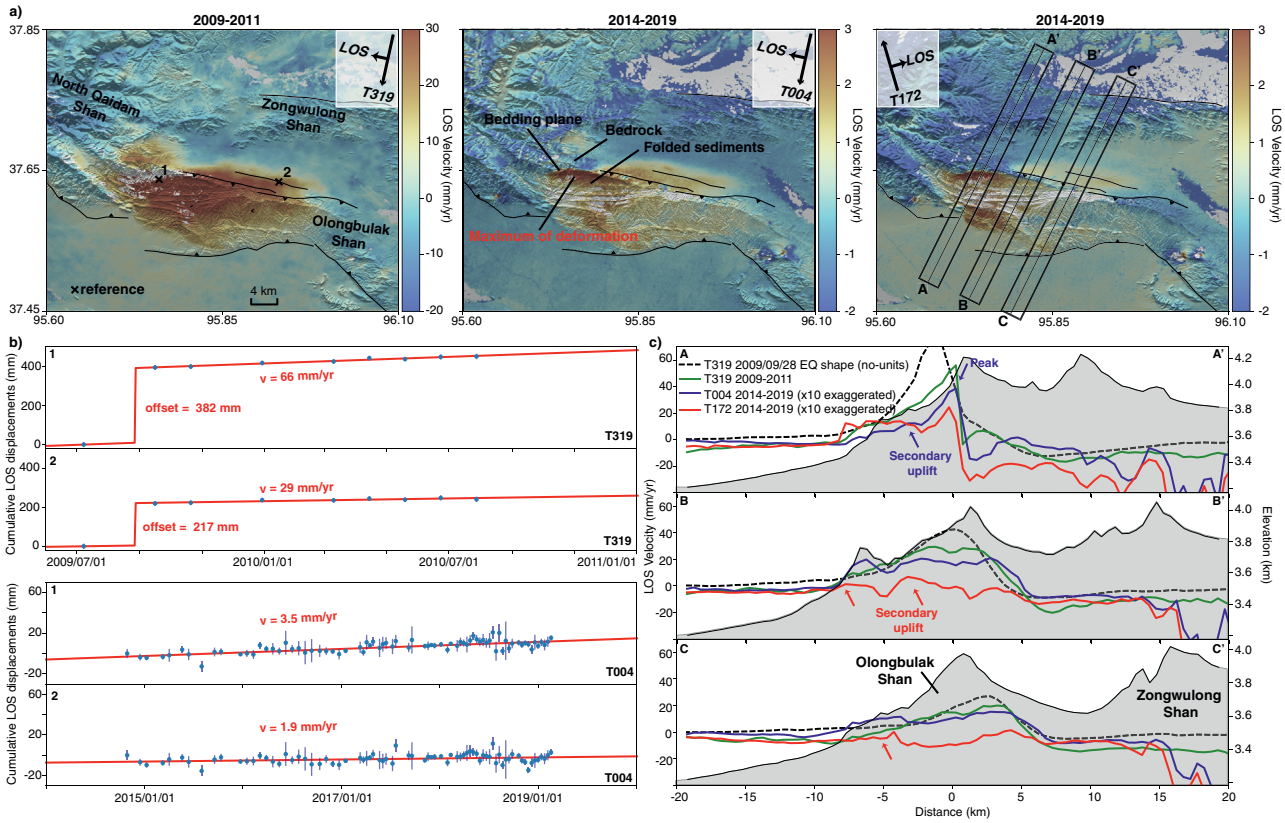

Figure 3. Post-seismic ground deformation following the 2009 Haixi earthquake. (a) Velocity maps for the 2009–2011 period extracted from Envisat descending track 319 (left), for the 2014–2019 period extracted from Sentinel-1 descending track 004 (middle) and for the 2014–2019 period extracted from Sentinel-1 ascending track 172 (right). (b) Time series displacements from 2009 to 2011 (top), determined for Envisat on descending track 319, and from 2014 to 2019 (Bottom), estimated for Sentinel-1 on descending track 004, for two pixels marked by crosses in (a). (c) Three 40-km-long LOS profiles, marked AA', BB', and CC' in panel (a), extracted from the Envisat descending velocity map from 2009 to 2011 (green lines), the Sentinel-1 descending velocity map from 2014 to 2019 (blue lines) and the Sentinel-1 ascending velocity map from 2014-2019 (red lines). The profiles are average over velocities in a swath of 4 km wide. Note that, for comparison, the Sentinel-1 velocities are 10 times vertically exaggerated. The reduced coseismic surface displacement (in mm) is also shown by dashed black line on the three profiles for comparison with the post-seismic velocities (in mm/yr).

2. Data and Method

2.1. Interferometric Synthetic Aperture Radar Data Processing

We used the three Envisat time series data along three ~300-km-long and 100-km-wide overlapping tracks (descending tracks 319, 047, and ascending track 455) between 2003 and 2011, processed in Daout, Sudhaus, Kausch, et al. (2019) (Figure S3). Additionally, we processed three Sentinel-1 tracks (descending tracks 004 and ascending tracks 172 and 099) acquired in interferometric wide-swath mode (width of ~250 km) from 2014 to 2019 (Figure S2). The processing is carried out using the New Small Baselines Subset (NSBAS) processing chain (Doin, Lodge, et al., 2011, Doin, Twardzik, et al., 2015), which includes routines from the ROI_PAC software (Rosen et al., 2004) and precise azimuthal coregistration with the spectral diversity

Figure 2. Post-seismic ground deformation following the 2003 Delingha earthquake. (a) Velocity maps for the 2003–2006 period extracted from Envisat descending track 047 (left), for the 2006–2011 period extracted from Envisat descending track 047 (middle), and for the 2014–2019 period extracted from Sentinel-1 descending track 004 (right). (b) Same as panel (a) but for the 2003–2011 period extracted from Envisat ascending track 455 (left), for the 2014–2019 period extracted from Sentinel-1 ascending track 172 (middle) and for 2014–2019 period extracted from Sentinel-1 ascending track 099 (middle). (c) Time series displacements from 2003 to 2011 (left), determined using Envisat SAR data, and from 2014 to 2019 (right), from Sentinel-1 SAR data, for the pixel marked by a cross in (a) on the two descending tracks 047 and 004. (d) Top: 40-km-long and 4-km-wide LOS profiles, marked AA' in panel (b), extracted through the Envisat ascending velocity map for 2003–2011 (orange lines) and the Sentinel-1 ascending velocity maps for 2014–2019 (red and brown lines). Bottom: Same LOS profile, but extracted through the Envisat descending velocity map from 2003 to 2006 (cyan lines), the Envisat descending velocity map from 2006 to 2011 (purple lines) and the Sentinel-1 descending velocity map from 2014-2019 (blue lines). Note that, for comparison, the 2014–2019 Sentinel-1 velocities and the 2006–2011 Envisat velocities are three times vertically exaggerated.

21699356, 2021, 3, Downloaded from https://agupubs.onlinelibrary.wiley.com/doi/10.1029/2020JB021241 by Cochrane France, Wiley Online Library on [10/03/2024]. See the Terms and Conditions (https://onlinelibrary.wiley.com/terms-and-conditions) on Wiley Online Library for rules of use; OA articles are governed by the applicable Creative Commons License

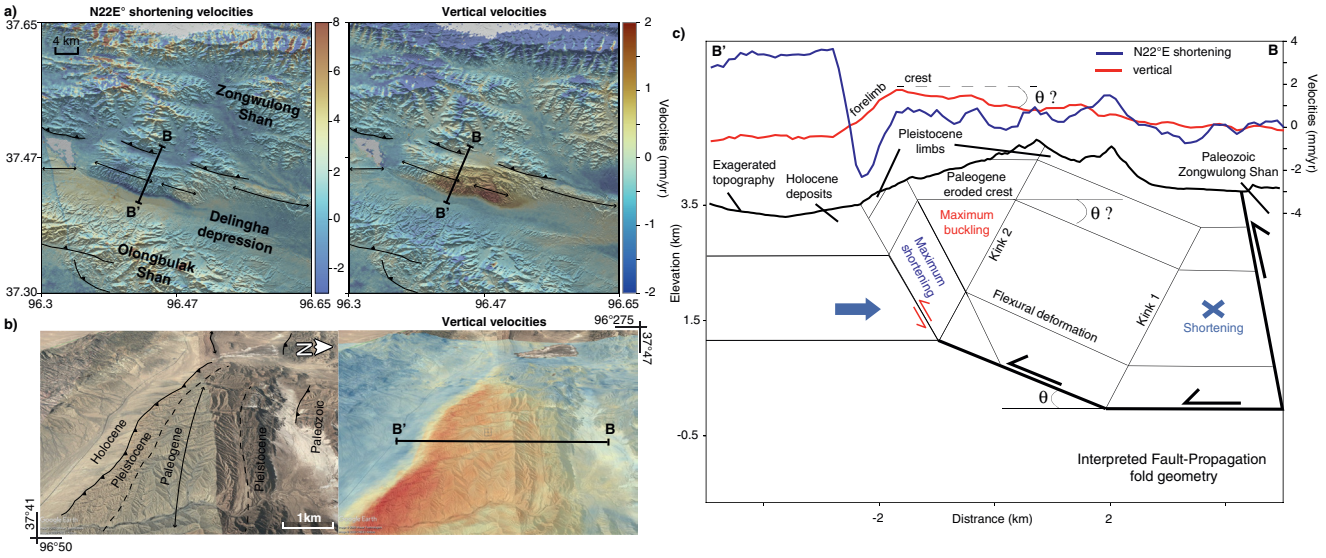

Figure 4. (a) N22°E shortening and vertical decomposition of the velocity of the Delingha earthquake area in Figure 2 obtained from Sentinel-1 post-seismic LOS velocities for ascending tracks 172 and 099 and descending track 004. Figure extend is as Figure 2. (b) Google-Earth imagery with interpreted geomorphological structures side-by-side with the enlargement of the vertical velocities of (a). Mapped active thrust faults are denoted by solid triangles in the hanging wall. The axe (black arrow) and limbs (dashed lines) of the anticline is inferred from the geomorphology. (c) Topography (black line) and surface velocity profiles (N22°E shortening in blue, vertical in red) with interpreted structural cross-section sketches. Shortening gradients illuminate the inferred location of the tip of the blind thrusts and anticline forelimb, while maximal vertical gradients are located along the inferred folds crest and forelimb. We interpret the shortening and vertical post-seismic velocities as due to simple fault-propagation fold underlying the Delingha anticline.

technique for Sentinel-1 data (Grandin, 2015; Grandin, Klein, et al., 2016; Métois et al., 2020). In order to avoid possible biases linked to the inclusion of short temporal baselines (Ansari et al., 2020), we include interferograms with both short and long temporal baselines in the analysis (Figure S3) that we successfully unwrap by applying empirical atmospheric corrections before unwrapping and by imposing an unwrapping

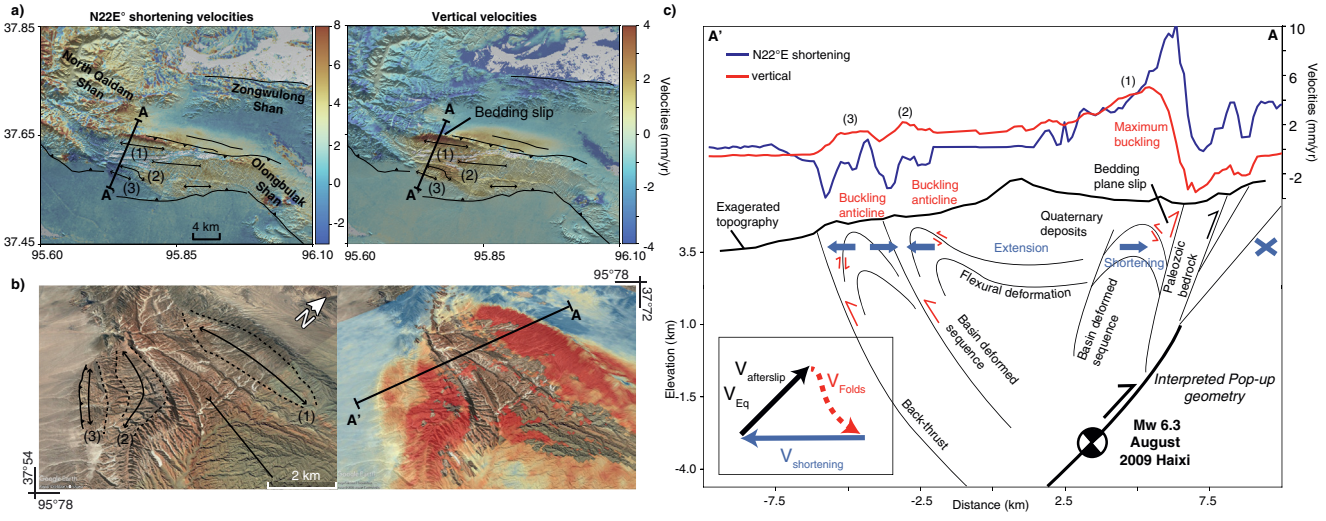

Figure 5. (a) N22 E shortening and vertical decomposition of the velocity of the Haixi earthquakes area in Figure 3 obtained from Sentinel-1 post-seismic LOS velocities for ascending track 172 and descending track 004. Figure extend is as Figure 3. (b) Google-Earth imagery with interpreted geomorphological structures side-by-side with the enlargement of the vertical velocities of (a). Mapped active thrust faults are denoted by solid triangles in the hanging wall. The axes (black arrows) and limbs (dashed lines) of the three anticlines are inferred from the geomorphology. (c) Topography (black line) and surface velocity profiles (N22°E shortening in blue, vertical in red) with interpreted structural cross-section sketches. We infer complex imbricated folds that underlain the Olongbulak pop-up structure. Inserts at the bottom left show interpreted conceptual conservation of motion vectors across the fault-system, where the faults and associated folds move at different periods of the seismic cycle.

21699356, 2021, 3, Downloaded from https://agupubs.onlinelibrary.wiley.com/doi/10.1029/2020JB021241 by Cochrane France, Wiley Online Library on [10/03/2024]. See the Terms and Conditions (https://onlinelibrary.wiley.com/terms-and-conditions) on Wiley Online Library for rules of use; OA articles are governed by the applicable Creative Commons License

21699356, 2021, 3, Downloaded from https://agupubs.onlinelibrary.wiley.com/doi/10.1029/2020JB021241 by Cochrane France, Wiley Online Library on [10/03/2024]. See the Terms and Conditions (https://onlinelibrary.wiley.com/terms-and-conditions) on Wiley Online Library for rules of use; OA articles are governed by the applicable Creative Commons License

path that start from more coherent areas and expand progressively into lower coherence (Grandin, Doin, et al., 2012).

After unwrapping, we re-introduce the empirical corrections that had been applied on the wrapped phase and construct cumulative time series on a pixel-by-pixel basis with the NSBAS method (Doin, Twardzik, et al., 2015; López-Quiroz et al., 2009). Residual unwrapping errors are first detected by visual inspection on interferograms or with high phase misclosure computed from the time series analysis (Doin, Lodge, et al., 2011; López-Quiroz et al., 2009). Errors are then corrected by imposing high-priority paths during a new unwrapping iteration. As part of the time series analysis, remaining unwrapping errors are further automatically identified and resolved using an iterative technique (López-Quiroz et al., 2009). In order to improve the referencing estimation and exclude surface periglacial processes from this analysis, we then, mask all pixels showing in the timeline of ground deformation, seasonal displacements higher than 3.5 mm associated with frost heave and thaw settlement of the permafrost active layer (Daout, Dini, Haeberli, et al., 2020). Cumulative LOS displacements (LOS(t)) from both Envisat and Sentinel-1 data are, subsequently corrected for tropospheric effects using the ERA-5 atmospheric model provided by ECMWF (Doin, Lasserre, et al., 2009; Jolivet et al., 2011), and referred to an 100 × 100 pixels area within the Qaidam basin of low elevation, low deformation gradient and high coherence. Afterward, in order to map and quantify the spatio-temporal strain evolution and associated uncertainties, we proceed to a simple linear parametric decomposition of the co-seismic and post-seismic ground deformations for the two earthquake areas.

2.2. Parametric Decomposition

Sentinel-1 ascending and descending tracks 004, 172, and 099 are first decomposed, assuming zero displacement during the first acquisition, into a single linear trend from 2014 to 2019 ($V_{2014-2019}$ in mm/yr) in both rupture areas (Figure S4):

$$LOS_{14-19}(t) = V_{14-19}t, \tag{1}$$

where t is the SAR acquisition time. In order to quantify the spatio-temporal evolution of the post-seismic strain release after the 17 April 2003 Delingha earthquake, we prescribe, for track 047, two linear trends from 2003 to 2006 (V_{03-06}) and from 2006 to 2011 (V_{06-11}) (Figure 2):

$$LOS^{desc}_{03-11}(t) \quad = V_{03-06}t \quad for \;\; 2003 \le t \le 2006, \tag{2}$$

$$= V_{06-11}t \quad for \;\; t > 2006 \tag{3}$$

By dividing the 2003–2011 time series data set into two distinct velocity periods, we avoid imposing any logarithmic or exponential post-seismic relationship on the data for descending track 047 (Figure 2). However, due to the poor temporal resolution of ascending track 455 (9 acquisitions only for this track) and the presence of only two acquisitions after the August 2009 Haixi earthquake, we only prescribe a single linear trend from 2003 to 2011 (V_{03-11}, in mm/yr) to extract the average strain rate around the Delingha earthquake area in ascending geometry (Figure 2):

$$LOS^{asc}_{03-11}(t) = V_{03-11}t. \tag{4}$$

Independently, as the 28 August 2009 Haixi earthquake was imaged by the Envisat descending track 319, we impose for this time series two basic functions:

$$LOS^{desc}_{09-11}(t) = V_{09-11}t + A_{09} * H(t - t_{09}), \tag{5}$$

where t_{09}, the timing of the 2009 earthquake; H, the Heaviside function; and A_{09} and V_{09-11} correspond to the amplitude of the August 2009 coseismic surface displacements (in mm) and the mean velocity from 2009 to 2011 (in mm/yr), respectively (Figure 3). The 10 November 2008 earthquake occurred south of the Olongbulak Shan with a depth of ~12 km and produced short-term and low-amplitude down-dip afterslip (Daout, Steinberg, Isken, et al., 2020). Conversely, the 28 August 2009 shallow event occurred at a depth of ~5 km and produced afterslip around the co-seismic area (Daout, Steinberg, Isken, et al., 2020; Elliott, Parsons, et al., 2011; Liu, Xu, Li, et al., 2016) (Figure 1b). Despite the deep origin of the 2008 post-seismic,

21699356, 2021, 3, Downloaded from https://agupubs.onlinelibrary.wiley.com/doi/10.1029/2020JB021241 by Cochrane France, Wiley Online Library on [10/03/2024]. See the Terms and Conditions (https://onlinelibrary.wiley.com/terms-and-conditions) on Wiley Online Library for rules of use; OA articles are governed by the applicable Creative Commons License

it is important to note that the short-term post-seismic observed in the Envisat data during the 2009–2011 period, might be a combination of the post-seismic surface displacements from both Haxi earthquakes.

2.3. Uncertainty Estimation

Two ascending and one descending Sentinel-1 track, with a total of 248 acquisitions, illuminate at a regional scale the LOS surface velocity from 2014 to 2019 over a 120,000 km^2 area of northeastern Tibet (Figure S4). Uncertainty maps, derived from the time series decomposition (Figure S5), are of 0.6 [0.4–0.8] mm/yr on average (with 95% confidence intervals), with a maximum uncertainty of up to ∼2 mm/yr in Qilian and Kunlun high ranges or at the bottom of some localized valleys. Those average low uncertainties, as well as the good agreement of the data within the profile in the overlapping area of the two ascending track 099 and 172 validates the quality of the results (Figure S6a). Histograms of differences of the overlap are approximatively Gaussian with mean close to zero and standard deviation of less than ∼0.5 mm/yr (Figure S6b). Descending track 004 also shows a good agreement with the regional Envisat velocity map from 2003 to 2011 obtained in Daout, Sudhaus, Kausch, et al. (2019) (Figures S6c and S7). However, the histogram of differences has an higher standard deviation for Envisat data, which can be explained by the larger noise of this data set due to the poorer temporal sampling in comparison to Sentinel-1 data and to the difference in time span (Figure S6d). Velocity maps also show some high velocity gradients toward the satellite in many basins bounded by high ranges (Figure S4), where uncertainties are also higher (Figure S5). Because interferograms have been corrected using the ERA-5 atmospheric model, and because of the good agreement between adjacent ascending tracks and the descending Envisat and Sentine-1 velocity maps, we discard large tropospheric residual signals (>∼1 mm/yr) in the velocity maps that arise from the oddly sampled seasonal stratified delays (Daout, Doin, Peltzer, Lasserre, et al., 2018; Doin, Lasserre, et al., 2009). We associate the apparent correlation with the topography as due to the effect of a long-term increase of water content within the sedimentary basins. Those interferometric synthetic aperture radar (InSAR) observations are in agreement with the water mass increase and gradual expansion of water levels of many lakes of North-East and Central Tibet of the past few decades, amplified by increase in surface air temperature and precipitation, melting of glaciers and thawing of ice-rich permafrost (Bibi et al., 2018; Daout, Dini, Haeberli, et al., 2020).

2.4. Forward Modeling

To get insights into deformation mechanisms and compare the observations with first-order dislocation models, we compute two-dimensional surface displacements, for a 20 km-long edge dislocation dipping at 35° to the north and embedded in an elastic half-space, using the formulations provided by Savage (1998) (Figure S8). Three synthetic surface displacements are plotted for variable locking depths (LD = 0, 5, or 10 km). We choose not to perform any inverse modeling to compare shortening and vertical surface displacement observations with the simplest fault geometry model, as we believe that a distributed fault model could fit almost any kind of surface deformation. We aim at demonstrating in the following sections that at least part of the signal can be explained by anelastic bulk deformation.

3. Results: Observational Constraints

To first-order, the LOS velocity maps (Figure S4) show, for both ascending and descending tracks, relative displacements away from the satellite (negative values) from the southern front of the Qilian and Qilian-Nan ranges to the North Qaidam thrust systems (within the North Qaidam ranges), and displacements toward the satellite (positive value) within the Qilian or Qilian-Nan ranges and within the Qaidam Basin, likely associated with the N22°E ∼4–6 mm/yr of shortening across the whole region, derived from GNSS measurements (Liang et al., 2013; Wang et al., 2017). Smaller-wavelength LOS gradients are correlated with Quaternary active fold-and-thrust belts on localized areas of the Qaidam Basin (Yin, Dang, Wang, et al., 2008; Yin, Dang, Zhang, et al., 2008) as across the Lenghu Anticlinorium, the south-dipping Aimunike Thrusts and north-dipping Xitieshan thrusts, or the Olongbulak and Delingha ranges (Figure S4). Assuming a tectonic origin for the deformation, the velocities are probably related to the slow aseismic shortening and uplift of segmented thrust faults and folds a few tens of kilometers long within the Qaidam basin. However, as the signals here are relatively small, we choose not to interpret them further. In the following sections, we

21699356, 2021, 3, Downloaded from https://agupubs.onlinelibrary.wiley.com/doi/10.1029/2020JB021241 by Cochrane France, Wiley Online Library on [10/03/2024]. See the Terms and Conditions (https://onlinelibrary.wiley.com/terms-and-conditions) on Wiley Online Library for rules of use; OA articles are governed by the applicable Creative Commons License

will focus on the two major deformation signals of the velocity map in Figure S4, which are linked to the post-seismic ground deformation following the 2003–2009 Qaidam earthquake sequence (Figure 1).

3.1. Post-seismic Deformation of the 2003 Delingha Earthquake

Decomposition of the Envisat time series of cumulative displacements for a 2003–2006 and 2006–2011 velocities (in mm/yr), as well as Sentinel-1 surface displacements into an average 2014–2019 velocity (in mm/yr), illuminate the evolution of the post-seismic deformation for the 2003 M_w 6.3 Delingha earthquake in descending (Figure 2a) and ascending geometries (Figure 2b). In both views, the post-seismic deformation evolves in time from the superposition of a 13 km-long and 6 km-wide sharp signal at the southern topographic front and a broader and long-wavelength signal, ~10 km further north, between 2003 and 2011, to a deformation pattern essentially concentrated across the Delingha anticline, between 2014 and 2019 (Figures 2a and 2b).

During the 2014–2019 period, both ascending and descending LOS surface displacements highlight a sharp signal of up to ~1.5 mm/yr that coincides with the topographic front of the Delingha anticline, in agreement with shallow deformation processes (Figures 2a and 2d). In comparison with the descending view, the peak of the ground deformation in ascending view is shifted a few kilometers southward (Figure 2d). This apparent difference in the peak of velocity gradient is likely due to the ~NS shortening sensitivity difference between the two geometries, which will be extracted in the following section.

While surface displacements are in good agreement with a logarithmic decay during the 2003–2011 period (as seen from Figure 2c and as modeled by Daout, Sudhaus, Kausch, et al., 2019), Sentinel-1 measurements suggest deformation rates do not follow a $\frac{1}{t}$ decay, as expected for deformation due to afterslip (e.g., Zhou et al., 2018) (Figure S9).

3.2. Post-seismic Deformation of the 2009 Haixi Earthquake

Decomposition of the Envisat time-series of cumulative surface displacements into a coseismic step in 2009 (in mm) and an average 2009–2011 velocity (in mm/yr), as well as the Sentinel-1 surface displacements into an average 2014–2019 velocity (in mm/yr), illuminate the spatio-temporal evolution of the 2009 Haixi post-seismic strain release (Figures 3a and S10). The co-seismic surface displacement pattern does not match the Olongbulak Shan topography (Figure S10). A spatial pattern similar to the 2009 Haixi earthquake is observed during the 2009–2011 aseismic period with Envisat, but extending slightly further north, as expected from shallow afterslip (Figures 3a and 3c and S10). During this short period after the earthquake, rates are 1 and 6 cm/yr in the hanging wall of the south-dipping fault that broke in 2009, with a sharp and narrow maximum peak in the northwestern part, and − 1-0 cm/yr, in a restricted area of the footwall of the south-dipping thrust (Figure 3). The 2009–2011 short-term post-seismic velocities show an along-strike segmentation of the strain release, which can also be modeled with three south-dipping thrust-fault (Daout, Steinberg, Isken, et al., 2020; Elliott, Parsons, et al., 2011).

The 2014–2019 surface velocity maps in ascending and descending views, show surface displacements patterns that differ from the Envisat co-seismic and post-seismic surface measurements from 2009 to 2011, with lobes toward the satellite matching almost perfectly the recent geological structures of the Olongbulak Shan, observed in satellite imagery (Figure 3a). For the descending geometry, a maximum surface LOS velocity of 4 and 5 mm/yr is measured on the north-western part of the uplifted ranges, at the contact between the Paleozoic bedrock in the north, and the deformed sedimentary sequences of the Olongbulak Shan (Guihua et al., 2013; Yin, Dang, Wang, et al., 2008). The descending western profile there (blue line in profile AA' of Figure 3c), suggests steep and asymmetric surface velocities with 2–3 mm/yr of subsidence in the footwall. Positive surface velocities in the hanging wall of the Sentinel-1 data (blue profile in Figure 3c) are slightly more distributed than in the 2009–2011 Envisat profile (green profile in Figure 3c), with secondary lobes 2.5 km south of the maximum peak. The ascending profile (red profile in Figure 3c), shows an even more distributed pattern, with a slower velocity peak of 2–3 mm/yr, in the northern front, shifted to the south in contrast to the descending geometry, and a ~8 km-wide LOS pattern, in the NS direction, toward

21699356, 2021, 3, Downloaded from https://agupubs.onlinelibrary.wiley.com/doi/10.1029/2020JB021241 by Cochrane France, Wiley Online Library on [10/03/2024]. See the Terms and Conditions (https://onlinelibrary.wiley.com/terms-and-conditions) on Wiley Online Library for rules of use; OA articles are governed by the applicable Creative Commons License

the satellite, which is correlated with the whole Olongbulak pop-up structure. On the two eastern profiles BB' and CC', post-seismic velocities during the 2014–2019 period are wider than the co-seismic surface displacements in both the two views, as for the 2009–2011 post-seismic velocities, but differ from the 2009–2011 period by showing additional short-wavelength peaks of LOS surface velocities toward the satellite in the southern part of the ranges. In other words, in contrast to the Envisat post-seismic measurements that suggest a single lobe of deformation that are in agreement with three shallow high-angle faults, Sentinel-1 observations indicate a more distributed signal, with deformation not only on the shallow northern part of the ranges, which broke during the 2009 event, but also across discrete sections of the southern part of the Olongbulak Shan.

4. Discussion

4.1. Inferred Structural and Kinematic Models

Both the Olongbulak and Delingha ranges have complicated surface expressions with both north-dipping and south-dipping scarps and with topography modified by erosion. Structural interpretations are, therefore, difficult for both areas, as illustrated by the variety of interpretations found in the literature (Fang et al., 2007; Guihua et al., 2013; Yin, Dang, Wang, et al., 2008). Geodetic measurement of surface displacements represents a good opportunity to show the utility of InSAR in elucidating structural models of fault-and-fold geometries. Decomposition of the LOS velocity signal into a N22°E horizontal and a vertical velocity (Figures 4 and 5, with associated uncertainties in Figures S11 and S12) is possible if we assume no ground deformation in the direction perpendicular to the shortening (Wright et al., 2004), which is here a reasonable assumption given the absence of strike-slip motion. From this decomposition, we observe that vertical surface displacements appear to affect the whole Delingha anticline and Olongbulak structure (Figures 4a and 4b and 5a and 5b). Maximum horizontal displacements rates of 0.5–1 cm/yr are higher within these two structures than in the surrounding areas of the North Qaidam thrust systems and higher than the average GNSS shortening rate of ~4–6 mm/yr, which is distributed across the whole North Qaidam fault system (Liang et al., 2013; Wang et al., 2017) (Figure S1), indicating that measured surface displacement rates represent transient deformation induced by the earthquakes. Given the moderate size of the shallow earthquakes and the short-wavelength of the post-seismic signal, we assume possible viscoelastic relaxation in the lower crust or mantle can be neglected.

The structural cross-section across the Delingha anticline shown in Figure 4c is inferred from the observed signal, our own geomorphological mapping, and available models from Yin, Dang, Wang, et al. (2008), Fang et al. (2007), and Daout, Sudhaus, Kausch, et al. (2019) (Figure S13). The Delingha fold shows sharp contacts between the truncated Pleistocene units on the southern sides of the fold and the Holocene deposits within the Delingha basin, in the footwall (Figure 4b, (Yin, Dang, Wang, et al., 2008)). The exhumed Paleogene soft sediments in the core of the anticline (black arrows in Figure 4b, left) are light-colored in comparison to the harder and more resistant Pleistocene limbs of the anticline. We interpret the folding of the sedimentary beds to be caused by the fault step up over a ramp (Figure 4c) (e.g., Walker, 2006). The geometry of the anticline is controlled by two kink bands, branching where the fault step up (kink 1 in Figure 4c), and at the end of the fault tip (kink 2) (Brandes & Tanner, 2014; Suppe & Medwedeff, 1990). When the fault propagates, the beds roll from a flat position into the steep kink bands.

Daout, Sudhaus, Kausch, et al. (2019) modeled the short-term logarithmic after-slip determined using Envisat data from 2003 to 2011 with a 2-dimensional segmented ramp-flat-ramp north-dipping structure that steepens as it approaches the surface (orange line in Figure S13). The absence of the broader long-wavelength signal, ~10 km north of the high-velocity gradient at the southern topography front, in the Sentinel-1 measurements, suggest that the deformation is essentially concentrated at shallower depth during 2014–2019. Horizontal surface displacements extracted from the 2014–2019 period across the Delingha anticline (blue profile in Figure 4c) are in agreement with movement of the hanging wall toward the south and with a shallow north-dipping thrust fault with steep horizontal gradient localized on the tip of the dislocation (Figure S8). However, an additional localized extension on the southern limb of the anticline is also measured, which is not in agreement with the dislocation models of Figure S8. We suggest that this observation might be the effect of the buckling of the crest, which collapses the southern limb and results in relative shortening across the blind north-dipping fault that is larger than the overall shortening over the region (Figure 4c).

21699356, 2021, 3, Downloaded from https://agupubs.onlinelibrary.wiley.com/doi/10.1029/2020JB021241 by Cochrane France, Wiley Online Library on [10/03/2024]. See the Terms and Conditions (https://onlinelibrary.wiley.com/terms-and-conditions) on Wiley Online Library for rules of use; OA articles are governed by the applicable Creative Commons License

In addition, contrary to what is expected from an elastic dislocation (Figure S8), no subsidence is observed north and south of the hanging wall (red profile in Figure 4c). Vertical velocity profiles show an asymmetric uplift, with steep velocity gradients in the southern limbs, which coincides with the region with high horizontal motion to the south, a maximum of uplift at the front of the crest, and a gently uplift gradient on the northern dipping limb. Kinematic fault-bend fold models predict that, slip on the dipping ramp produces uplift of the back-limb above the ramp alone, whereas fault-propagation and detachment fold model uplift the crest (Brandes & Tanner, 2014; Suppe, 1983). We propose that the measured vertical velocity with Sentinel-1 data corresponds to the long-term uplift of the fold, which is here consistent with a fold underlain by a north-dipping thrust fault (Brandes & Tanner, 2014; Daëron et al., 2007; Suppe, 1983; Walker, 2006), with a steep but eroded forelimb and a more gently dipping back-limb, as conceptually proposed in Figure 4c. The findings suggest that the 2003 coseismic rupture in the basement induced aseismic fault slip in the sedimentary cover, which has evolved from localized slip shortly after the event (during the 2003–2009 period, approximatively) to a more distributed deformation (during the 2014–2019 period, approximatively) across the anticline. This transient strain release is still ongoing in 2019, more than 16 years after the earthquake.

From our InSAR measurements and the structural cross-section of Yin, Dang, Wang, et al. (2008), Guihua et al. (2013) and Daout, Steinberg, Isken, et al. (2020), we infer for the Olongbulak pop-up, the structural cross-section of Figure 5c. From the inverted shortening rates (Figure 5a), the Olongbulak Shan is mainly moving to the north, with a concentration of the shortening gradient on the northwestern part of the range. However, a movement in the SW direction is also observed on the southwestern part of the system, highlighting the activity of the north-dipping branches, in the southern side of the Olongbulak range and some extension between the northern and southern side of the pop-up structure. Curiously, the N22°E velocity difference across the whole structure (i.e., the shortening) is close to zero (Figure 5c), which is in disagreement with elastic dislocation models (Figure S8). This absence of shortening motion in the far-field of the structure, in contrast to the observed motion within the structure, may indicate a motion driven from below with the vertical motion. From 2014 to 2019, vertical ground motion is observed across the whole ~10 km-large structure with three maxima that coincided with the three inferred anticlines, numbered (1), (2), and (3) in Figure 5b, from our own geomorphological analysis and bibliographic reviews (Elliott, Parsons, et al., 2011; Guihua et al., 2013; Yin, Dang, Wang, et al., 2008). Differences between ascending track 099 and descending track 004, due to the N22°E shortening (Figure 3a), are mainly observed in the northern part of the pop-up structure, where the LOS surface velocity is also sharp and asymmetric. Surface velocities there may be compatible with shallow aseismic slip on a south-dipping fault (Figure S8), located on the upward prolongation of the south-dipping and shallow 2009 rupture (Figure 5c). However, higher rates of surface velocities are located between the basin deformed sedimentary sequences of the Olongbulak range and the Paleozoic bedrock, north of it (Figure 5b). As we did not identify fault traces or folds in the satellite imagery where the maximum uplift is measured and as two different rock types are identified from the satellite imagery and from the geological mapping of Yin, Dang, Wang, et al. (2008), we interpret the high surface displacements here as due to bedding planes slip along the stratigraphic contacts between a major anticline to the south (marked 1) and the Paleozoic strata to the north. In this complex structure, with imbricated Cenozoic and Mesozoic strata and multiple folds of different ages, old bedding planes might have been reactivated as faults following more recent events, such as the 2009 south-dipping Haixi earthquake (Figure 5c).

In the southern part of the Olongbulak Shan, two secondary uplift lobes are colocated with the two identified southern anticlines, marked (2) and (3) (Figure 5a); small symmetric localized N22°E horizontal components are also observed there. The two folds show truncated geological units with sharp contacts on the southern sides between the uplifted rocks and the more recent deposits on the footwall (Figure 5b). Those two surface expressions are in agreement with two folds associated with shallow north-dipping faults. The exhumed soft sediments in the core of the two anticlines (black arrows in Figure 5b) are light-colored in comparison to the harder and more resistant rocks exposed on the two limbs of the folds (black dashed-lines in Figure 5b). Because of differential erosion, the back-limbs look steeper in comparison to the crest and the forelimbs (Figure 5b). Because the surface displacements coincide with the two fold morphologies and because the symmetric shortening signal is not in agreement with what would be expected from slip on thrust faults (Figure S8), we here again interpret the signal not as the direct result of slip along a north-dipping thrust structure, but as distributed fold-growth deformation of the upper layers induced by slip during the 2008–2009 Haixi events and afterslip following them. The deformation might be accommodated by

multiple mechanisms such as off-fault deformation along bedding planes or visco-plastic flexural shear creating mainly vertical uplift in combination with internal shearing with no net shortening across the whole structure. To conclude, the dip-angle between the main south-dipping thrust underlying the Olongbulak pop-up that ruptured during the 2009 Haixi earthquake (conceptual black arrow in Figure 5c, insert) and the horizontal shortening (conceptual blue arrow in Figure 5c, insert) creates a reverse north-dipping component of motion that must be accommodated during the seismic cycle either by seismic or aseismic deformation (conceptual red arrow in Figure 5c, insert). The measurements suggest that this vertical partitioning is, at least in part, compensated by aseismic post-seismic folding across the whole structure and localized along the anticlines observed in the geomorphology.

4.2. Aseismic Transient Phenomena

Since the discovery at different crustal depths of aseismic transient phenomena from observations made using geodetic networks, large efforts have been made by the geodetic and earthquake communities to better understand and locate these events occurring at low rupture speed and to improve the understanding of their interaction with earthquakes (e.g., Behr & Bürgmann, 2020; Collettini et al., 2011; Hawthorne et al., 2016; Obara & Hirose, 2006; Rousset et al., 2016; Socquet et al., 2017). The findings of this study illustrate that moderate earthquakes can trigger anelastic transient responses of the shallow crust, which lasts for decades. It shows that visco-plastic deformation can be produced in low strain regimes by moderate stress changes and at shallow depths. These observations may support weak fault zone models, documented both at shallow (e.g., Niemeijer & Spiers, 2005; Collettini et al., 2011) and greater depths (e.g., Behr & Bürgmann, 2020), where velocity-strengthening frictional behavior is enhanced by the presence of weak materials, such as phyllosilicate-rich meta-sediments or sediments, within heterogeneous fault zones. In those models, weak rocks or viscous matrix surround mafic and more competent lenses, and may accommodate the transient deformation by pressure solution, foliation-parallel sliding, viscous deformation and micro-folds (e.g., Collettini et al., 2011; Niemeijer & Spiers, 2005; Lavier et al., 2013; Reber et al., 2014). This study suggests that slow and transient aseismic events, detected both at shallow and greater depths during the inter- or post-seismic periods, might not be always linked with slip on a thin main fault or slab driving elastic deformation of the surrounding medium. On the contrary, they might also be associated with anelastic response of the medium itself, either triggered by an earthquake on the main adjacent fault-segment (post-seismic transients), or by a transient increase in stress concentrations within the more competent rocks of an heterogeneous shear zone (slow-slip transients). The increased number of InSAR satellite missions and the improved temporal resolution of new satellites open wide perspectives for accessing the lag between the co-seismic forcing and the anelastic response of the crust, and therefore better estimating the effective viscosity controlling those mechanisms.

5. Conclusion

The improved spatial and temporal sampling offered by the new generation of Sentinel-1 radar data in both ascending and descending geometries, has enabled us to resolve the vertical and shortening component across two fold-and-thrust belts in the Qaidam Basin, China. The study reveals a link between the post-seismic phase and the long-term geomorphology of the tectonic structures. We interpret the non-logarithmic long-term ground aseismic surface displacements observed up to 16 years after the seismic events as off-fault volumetric and anelastic deformation associated with active folding. In the two examples, co-seismic slip is translated into permanent deformation during the post-seismic phase through localized signals that match young anticlines observed in the morphology, and that cannot be simply explained by slip along faults driving elastic deformation of the medium. The results demonstrate, along with other observations and models (e.g., Ainscoe et al., 2017; Bonanno et al., 2017; Johnson, 2018), that it not always valid to assume that fold growth above blind reverse faults is co-seismic or that it is appropriate to model it by slip on a fault, because a significant part of the finite shortening may occur as distributed off-fault deformation (flexural slip, interbed flow, shearing) during the post-seismic or inter-seismic phases. The study highlights that the contribution of distributed deformation and slip-partitioning between secondary structures needs to be considered in earthquake cycle models, analyses of fault-related folds, and the assessments of earthquake hazard from surface measurements.

21699356, 2021, 3, Downloaded from https://agupubs.onlinelibrary.wiley.com/doi/10.1029/2020JB021241 by Cochrane France, Wiley Online Library on [10/03/2024]. See the Terms and Conditions (https://onlinelibrary.wiley.com/terms-and-conditions) on Wiley Online Library for rules of use; OA articles are governed by the applicable Creative Commons License

Data Availability Statement

All the InSAR products produced in this study (velocity maps and co-seismic map) are available online at https://webapps.bgs.ac.uk/services/ngdc/accessions/index.html#item161925. The Envisat SAR SLC data are provided by the European Space Agency (ESA) and can be acquired through an online proposal (https://earth.esa.int/web/guest/missions/esa-operational-eo-missions/envisat). Sentinel-1 SLC data are freely available online at https://scihub.copernicus.eu. Topographic data are provided by NASA and available also online at https://e4ftl01.cr.usgs.gov/.

Acknowledgments
This research was supported by the Natural Environment Research Council through the Looking into the Continents from Space (LiCS) large grant (NE/K011006/1) and the Center for the Observation and modeling of Earthquakes, Volcanoes and Tectonics (COMET). We thank the Editor Isabelle Manighetti, the Associate Editor Emma Hill, as well as Rishav Mallick and one anonymous reviewer for their valuable comments.

References

Ainscoe, E., Elliott, J., Copley, A., Craig, T., Li, T., Parsons, B., & Walker, R. (2017). Blind thrusting, surface folding, and the development of geological structure in the Mw 6.3 2015 Pishan (China) earthquake. *Journal of Geophysical Research: Solid Earth*, *122*(11), 9359–9382. https://doi.org/10.1002/2017jb014268

Ansari, H., De Zan, F., & Parizzi, A. (2020). *Study of systematic bias in measuring surface deformation with SAR interferometry*. IEEE.

Barnhart, W. D., Brengman, C. M., Li, S., & Peterson, K. E. (2018). Ramp-flat basement structures of the Zagros Mountains inferred from co-seismic slip and afterslip of the 2017 Mw 7.3 Darbandikhan, Iran/Iraq earthquake. *Earth and Planetary Science Letters*, *496*, 96–107. https://doi.org/10.1016/j.epsl.2018.05.036

Barnhart, W. D., Lohman, R. B., & Mellors, R. J. (2013). Active accommodation of plate convergence in Southern Iran: Earthquake locations, triggered aseismic slip, and regional strain rates. *Journal of Geophysical Research: Solid Earth*, *118*(10), 5699–5711. https://doi.org/10.1002/jgrb.50380

Behr, W., & Bürgmann, R. (2020). What's down there? The structures, materials and environment of deep-seated tremor and slip. *Philosophical Transactions of the Royal Society*.

Belabbès, S., Meghraoui, M., Çakir, Z., & Bouhadad, Y. (2009). InSAR analysis of a blind thrust rupture and related active folding: The 1999 Ain Temouchent earthquake (Mw 5.7, Algeria) case study. *Journal of Seismology*, *13*(4), 421–432. https://doi.org/10.1007/s10950-008-9135-x

Bibi, S., Wang, L., Li, X., Zhou, J., Chen, D., & Yao, T. (2018). Climatic and associated cryospheric, biospheric, and hydrological changes on the Tibetan Plateau: A review. *International Journal of Climatology*, *38*, e1–e17. https://doi.org/10.1002/joc.5411

Bonanno, E., Bonini, L., Basili, R., Toscani, G., & Seno, S. (2017). How do horizontal, frictional discontinuities affect reverse fault-propagation folding? *Journal of Structural Geology*, *102*, 147–167. https://doi.org/10.1016/j.jsg.2017.08.001

Brandes, C., & Tanner, D. C. (2014). Fault-related folding: A review of kinematic models and their application. *Earth-Science Reviews*, *138*, 352–370. https://doi.org/10.1016/j.earscirev.2014.06.008

Collettini, C., Niemeijer, A., Viti, C., Smith, S. A., & Marone, C. (2011). Fault structure, frictional properties and mixed-mode fault slip behavior. *Earth and Planetary Science Letters*, *311*(3–4), 316–327. https://doi.org/10.1016/j.epsl.2011.09.020

Copley, A. (2014). Postseismic afterslip 30 years after the 1978 Tabas-e-Golshan (Iran) earthquake: Observations and implications for the geological evolution of thrust belts. *Geophysical Journal International*, *197*(2), 665–679. https://doi.org/10.1093/gji/ggu023

Daëron, M., Avouac, J.-P., & Charreau, J. (2007). Modeling the shortening history of a fault tip fold using structural and geomorphic records of deformation. *Journal of Geophysical Research*, *112*(B3). https://doi.org/10.1029/2006jb004460

Daout, S., Barbot, S., Peltzer, G., Doin, M.-P., Liu, Z., & Jolivet, R. (2016). Constraining the kinematics of metropolitan Los Angeles faults with a slip-partitioning model. *Geophysical Research Letters*.

Daout, S., Dini, B., Haeberli, W., Doin, M.-P., & Parsons, B. (2020). Ice loss in the Northeastern Tibetan Plateau permafrost as seen by 16 yr of ESA SAR missions. *Earth and Planetary Science Letters*, *545*, 116404. https://doi.org/10.1016/j.epsl.2020.116404

Daout, S., Doin, M.-p., Peltzer, G., Lasserre, C., Socquet, A., Volat, M., & Sudhaus, H. (2018). Strain partitioning and present-day fault kinematics in NW Tibet from Envisat SAR interferometry. *Journal of Geophysical Research: Solid Earth*, *123*(3), 2462–2483. https://doi.org/10.1002/2017JB015020

Daout, S., Steinberg, A., Isken, M. P., Heimann, S., & Sudhaus, H. (2020). Illuminating the spatio-temporal evolution of the 2008–2009 Qaidam earthquake sequence with the joint use of InSAR time series and teleseismic data. *Remote Sensing*, *12*(17), 2850. https://doi.org/10.1016/j.epsl.2020.116404

Daout, S., Sudhaus, H., Kausch, T., Steinberg, A., & Dini, B. (2019). Interseismic and postseismic shallow creep of the North Qaidam Thrust faults detected with a multitemporal InSAR analysis. *Journal of Geophysical Research: Solid Earth*, *124*(7), 7259–7279. https://doi.org/10.1029/2019jb017692

Davis, D., Suppe, J., & Dahlen, F. (1983). Mechanics of fold-and-thrust belts and accretionary wedges. *Journal of Geophysical Research*, *88*(B2), 1153–1172. https://doi.org/10.1029/jb088ib02p01153

Doin, M.-P., Lasserre, C., Peltzer, G., Cavalié, O., & Doubre, C. (2009). Corrections of stratified tropospheric delays in SAR interferometry: Validation with global atmospheric models. *Journal of Applied Geophysics*, *69*, 35–50. https://doi.org/10.1016/j.jappgeo.2009.03.010

Doin, M.-P., Lodge, F., Guillaso, S., Jolvet, R., Lasserre, C., Ducret, G., et al. (2011). Presentation of the small baseline NSBAS processing chain on a case example: The Etna deformation monitoring from 2003 to 2010 using Envisat data. *Proc. ESA Fringe*.

Doin, M.-P., Twardzik, C., Ducret, G., Lasserre, C., Guillaso, S., & Jianbao, S. (2015). InSAR measurement of the deformation around Siling Co Lake: Inferences on the lower crust viscosity in central Tibet. *Journal of Geophysical Research: Solid Earth*, *120*(7), 5290–5310. https://doi.org/10.1002/2014jb011768

Dolan, J. F., & Avouac, J.-P. (2007). Introduction to special section: Active fault-related folding: Structural evolution, geomorphologic expression, paleoseismology, and seismic hazards. *Journal of Geophysical Research*, *112*(B3). https://doi.org/10.1029/2007jb004952

Elliott, J., Bergman, E., Copley, A., Ghods, A., Nissen, E., Oveisi, B., et al. (2015). The 2013 mw 6.2 Khaki-Shonbe (Iran) earthquake: Insights into seismic and aseismic shortening of the Zagros sedimentary cover. *Earth and Space Science*, *2*(11), 435–471. https://doi.org/10.1002/2015ea000098

Elliott, J., Jolivet, R., González, P., Avouac, J.-P., Hollingsworth, J., Searle, M., & Stevens, V. (2016). Himalayan megathrust geometry and relation to topography revealed by the Gorkha earthquake. *Nature Geoscience*, *9*(2), 174–180. https://doi.org/10.1038/ngeo2623

Elliott, J., Parsons, B., Jackson, J., Shan, X., Sloan, R., & Walker, R. (2011). Depth segmentation of the seismogenic continental crust: The 2008 and 2009 Qaidam earthquakes. *Geophysical Research Letters*, *38*(6). https://doi.org/10.1029/2011gl046897

21699356, 2021, 3, Downloaded from https://agupubs.onlinelibrary.wiley.com/doi/10.1029/2020JB021241 by Cochrane France, Wiley Online Library on [10/03/2024]. See the Terms and Conditions (https://onlinelibrary.wiley.com/terms-and-conditions) on Wiley Online Library for rules of use; OA articles are governed by the applicable Creative Commons License

Fang, X., Zhang, W., Meng, Q., Gao, J., Wang, X., King, J., et al. (2007). High-resolution magnetostratigraphy of the Neogene Huaitoutala section in the eastern Qaidam Basin on the NE Tibetan Plateau, Qinghai Province, China and its implication on tectonic uplift of the NE Tibetan plateau. *Earth and Planetary Science Letters*, *258*(1–2), 293–306. https://doi.org/10.1016/j.epsl.2007.03.042

Feng, W. (2015). *Modelling co-and post-seismic displacements revealed by inSAR, and their implications for fault behaviour* (Unpublished doctoral dissertation). University of Glasgow.

Fielding, E. J., Wright, T. J., Muller, J., Parsons, B. E., & Walker, R. (2004). Aseismic deformation of a fold-and-thrust belt imaged by synthetic aperture radar interferometry near Shahdad, southeast Iran. *Geology*, *32*(7), 577–580. https://doi.org/10.1130/g20452.1

Gonzalez-Mieres, R., & Suppe, J. (2006). Relief and shortening in detachment folds. *Journal of Structural Geology*, *28*(10), 1785–1807. https://doi.org/10.1016/j.jsg.2006.07.001

Grandin, R. (2015). Interferometric processing of SLC Sentinel-1 TOPS data. *Fringe*, *2015*(731), 36. https://doi.org/10.1109/TGRS.2015.2497902

Grandin, R., Doin, M.-P., Bollinger, L., Pinel-Puysségur, B., Ducret, G., Jolivet, R., & Sapkota, S. N. (2012). Long-term growth of the Himalaya inferred from interseismic InSAR measurement. *Geology*, *40*(12), 1059–1062. https://doi.org/10.1130/g33154.1

Grandin, R., Klein, E., Métois, M., & Vigny, C. (2016). Three-dimensional displacement field of the 2015 mw8. 3 illapel earthquake (chile) from across-and along-track sentinel-1 tops interferometry. *Geophysical Research Letters*, *43*(6), 2552–2561. https://doi.org/10.1002/2016gl067954

Guihua, C., Xiwei, X., Ailan, Z., Xiaoqing, Z., Renmao, Y., Klinger, Y., & Nocquet, J.-M. (2013). Seismotectonics of the 2008 and 2009 Qaidam earthquakes and its implication for regional tectonics. *Acta Geologica Sinica-English Edition*, *87*(2), 618–628. https://doi.org/10.1111/1755-6724.12072

Guilbaud, C., Simoes, M., Barrier, L., Laborde, A., Van der Woerd, J., Li, H., et al. (2017). Kinematics of active deformation across the western Kunlun mountain range (Xinjiang, China) and potential seismic hazards within the southern Tarim Basin. *Journal of Geophysical Research: Solid Earth*, *122*(12), 10–398. https://doi.org/10.1002/2017jb014069

Hawthorne, J. C., Bostock, M. G., Royer, A. A., & Thomas, A. M. (2016). Variations in slow slip moment rate associated with rapid tremor reversals in Cascadia. *Geochemistry, Geophysics, Geosystems*, *17*(12), 4899–4919. https://doi.org/10.1002/2016gc006489

Huang, W.-J., & Johnson, K. M. (2016). A fault-cored anticline boundary element model incorporating the combined fault slip and buckling mechanisms. *Terrestrial, Atmospheric and Oceanic Sciences*, *27*(1). https://doi.org/10.3319/tao.2015.06.18.01(tt)

Johnson, K. M. (2018). Growth of fault-cored anticlines by flexural slip folding: Analysis by boundary element modeling. *Journal of Geophysical Research: Solid Earth*, *123*(3), 2426–2447. https://doi.org/10.1002/2017jb014867

Jolivet, R., Grandin, R., Lasserre, C., Doin, M.-P., & Peltzer, G. (2011). Systematic InSAR tropospheric phase delay corrections from global meteorological reanalysis data. *Geophysical Research Letters*, *38*(17). https://doi.org/10.1029/2011gl048757

Lavier, L. L., Bennett, R. A., & Duddu, R. (2013). Creep events at the brittle ductile transition. *Geochemistry, Geophysics, Geosystems*, *14*(9), 3334–3351. https://doi.org/10.1002/ggge.20178

Liang, S., Gan, W., Shen, C., Xiao, G., Liu, J., Chen, W., et al. (2013). Three-dimensional velocity field of present-day crustal motion of the Tibetan Plateau derived from GPS measurements. *Journal of Geophysical Research*, *118*(10), 5722–5732. https://doi.org/10.1002/2013jb010503

Liu, Y., Xu, C., Li, Z., Wen, Y., Chen, J., & Li, Z. (2016). Time-dependent afterslip of the 2009 mw 6.3 Dachaidan earthquake (China) and viscosity beneath the Qaidam basin inferred from postseismic deformation observations. *Remote Sensing*, *8*(8), 649.

Liu, Y., Xu, C., Wen, Y., & Fok, H. S. (2015). A new perspective on fault geometry and slip distribution of the 2009 Dachaidan Mw 6.3 earthquake from InSAR observations. *Sensors*, *15*(7), 16786–16803.

Liu, Y., Xu, C., Wen, Y., & Li, Z. (2016). Post-seismic deformation from the 2009 mw 6.3 dachaidan earthquake in the northern Qaidam basin detected by small baseline subset InSAR technique. *Sensors*, *16*(2), 206.

López-Quiroz, P., Doin, M.-P., Tupin, F., Briole, P., & Nicolas, J.-M. (2009). Time series analysis of Mexico City subsidence constrained by radar interferometry. *Journal of Applied Geophysics*, *69*(1), 1–15.

Mackenzie, D., Elliott, J., Altunel, E., Walker, R., Kurban, Y., Schwenninger, J.-L., & Parsons, B. (2016). Seismotectonics and rupture process of the Mw 7.1 2011 Van reverse-faulting earthquake, eastern Turkey, and implications for hazard in regions of distributed shortening. *Geophysical Journal International*, *206*(1), 501–524.

Mariniere, J., Nocquet, J., Beauval, C., Champenois, J., Audin, L., Alvarado, A., et al. (2020). Geodetic evidence for shallow creep along the Quito fault, Ecuador. *Geophysical Journal International*, *220*(3), 2039–2055.

Medwedeff, D. A., & Suppe, J. (1997). Multibend fault-bend folding. *Journal of Structural Geology*, *19*(3–4), 279–292.

Métois, M., Benjelloun, M., Lasserre, C., Grandin, R., Barrier, L., Dushi, E., & Koçi, R. (2020). Subsidence associated with oil extraction, measured from time series analysis of sentinel-1 data: case study of the Patos-Marinza oil field, Albania. *Solid Earth*, *11*(2).

Meyer, B., Tapponnier, P., Bourjot, L., Metivier, F., Gaudemer, Y., Peltzer, G., et al. (1998). Crustal thickening in Gausu-Qinghai, lithospheric mantle subduction, and oblique, strike-slip controlled growth of the Tibet Plateau. *Geophysical Journal International*, *135*.

Niemeijer, A. R., & Spiers, C. J. (2005). Influence of phyllosilicates on fault strength in the brittle-ductile transition: Insights from rock analogue experiments. *Geological Society, London, Special Publications*, *245*(1), 303–327.

Nissen, E., Ghorashi, M., Jackson, J., Parsons, B., & Talebian, M. (2007). The 2005 Qeshm island earthquake (Iran). A link between buried reverse faulting and surface folding in the Zagros simply folded belt? *Geophysical Journal International*, *171*(1), 326–338.

Obara, K., & Hirose, H. (2006). Non-volcanic deep low-frequency tremors accompanying slow slips in the southwest Japan subduction zone. *Tectonophysics*, *417*(1–2), 33–51. https://doi.org/10.1016/j.tecto.2005.04.013

Pang, J., Yu, J., Zheng, D., Wang, W., Ma, Y., Wang, Y., et al. (2019). Neogene expansion of the Qilian Shan, north Tibet: Implications for the dynamic evolution of the Tibetan plateau. *Tectonics*, *38*(3), 1018–1032.

Reber, J. E., Hayman, N. W., & Lavier, L. L. (2014). Stick-slip and creep behavior in lubricated granular material: Insights into the brittle-ductile transition. *Geophysical Research Letters*, *41*(10), 3471–3477.

Rosen, P. A., Hensley, S., Peltzer, G., & Simons, M. (2004). Updated repeat orbit interferometry package released. *Eos, Transactions American Geophysical Union*, *85*(5), 47.

Rousset, B., Jolivet, R., Simons, M., Lasserre, C., Riel, B., Milillo, P., et al. (2016). An aseismic slip transient on the North Anatolian Fault. *Geophysical Research Letters*, *43*(7), 3254–3262.

Sathiakumar, S., Barbot, S., & Hubbard, J. (2020). Earthquake cycles in fault-bend folds. *Journal of Geophysical Research: Solid Earth*, e2019JB018557.

Savage, J. (1998). Displacement field for an edge dislocation in a layered half-space. *Journal of Geophysical Research: Solid Earth*, *103*(B2), 2439–2446.

21699356, 2021, 3, Downloaded from https://agupubs.onlinelibrary.wiley.com/doi/10.1029/2020JB021241 by Cochrane France, Wiley Online Library on [10/03/2024]. See the Terms and Conditions (https://onlinelibrary.wiley.com/terms-and-conditions) on Wiley Online Library for rules of use; OA articles are governed by the applicable Creative Commons License

Shaw, J. H., Connors, C. D., Suppe, J. (2005). Seismic interpretation of contractional fault-related folds: An AAPG seismic atlas (Vol. 53). American Association of Petroleum Geologists Tulsa.

Shaw, J. H., Plesch, A., Dolan, J. F., Pratt, T. L., & Fiore, P. (2002). Puente hills blind-thrust system, Los Angeles, California. *Bulletin of the Seismological Society of America*, *92*(8), 2946–2960.

Socquet, A., Valdes, J. P., Jara, J., Cotton, F., Walpersdorf, A., Cotte, N., et al. (2017). An 8 month slow slip event triggers progressive nucleation of the 2014 Chile megathrust. *Geophysical Research Letters*, *44*(9), 4046–4053.

Stein, R. S., & King, G. C. (1984). Seismic potential revealed by surface folding: 1983 Coalinga, California, earthquake. *Science*, *224*(4651), 869–872.

Sun, C.-H., Xu, F., Yang, Y.-B., Qian, R.-Y., & Meng, X.-H. (2012). Focal mechanism solutions of the 2003 Delingha, Qinghai M6.7 earthquake sequence and their tectonic implications. *Chinese Journal of Geophysics*, *55*(6), 680–688.

Suppe, J. (1983). Geometry and kinematics of fault-bend folding. *American Journal of Science*, *283*(7), 684–721.

Suppe, J., & Medwedeff, D. A. (1990). Geometry and kinematics of fault-propagation folding. *Eclogae Geologicae Helvetiae*, *83*(3), 409–454.

Tapponnier, P., Meyer, B., Avouac, J. P., Peltzer, G., Gaudemer, Y., & Shunmin, G., et al. (1990). Active thrusting and folding in the Qilian Shan, and decoupling between upper crust and mantle in northeastern Tibet. *Earth and Planetary Science Letters*, *97*(3–4), 382–403.

Tapponnier, P., Zhiqin, X., Roger, F., Meyer, B., Arnaud, N., Wittlinger, G., & Jingsui, Y. (2001). Oblique stepwise rise and growth of the Tibet Plateau. *Science*, *294*(5547), 1671–1677.

Tizzani, P., Castaldo, R., Solaro, G., Pepe, S., Bonano, M., Casu, F., et al. (2013). New insights into the 2012 Emilia (Italy) seismic sequence through advanced numerical modeling of ground deformation InSAR measurements. *Geophysical Research Letters*, *40*(10), 1971–1977. https://doi.org/10.1002/grl.50290

Veloza, G., Taylor, M., Mora, A., & Gosse, J. (2015). Active mountain building along the eastern Colombian Subandes: A folding history from deformed terraces across the Tame anticline, Llanos Basin. *Bulletin*, *127*(9–10), 1155–1173.

Walker, R. T. (2006). A remote sensing study of active folding and faulting in southern Kerman province, SE Iran. *Journal of Structural Geology*, *28*(4), 654–668.

Wang, W., Qiao, X., Yang, S., & Wang, D. (2017). Present-day velocity field and block kinematics of Tibetan Plateau from GPS measurements. *Geophysical Journal International*, *208*(2), 1088–1102.

Ward, S. N., & Valensise, G. (1994). The Palos Verdes terraces, California: Bathtub rings from a buried reverse fault. *Journal of Geophysical Research*, *99*(B3), 4485–4494. https://doi.org/10.1029/93jb03362

Whipple, K. X., Shirzaei, M., Hodges, K. V., & Arrowsmith, J. R. (2016). Active shortening within the Himalayan orogenic wedge implied by the 2015 Gorkha earthquake. *Nature Geoscience*, *9*(9), 711–716.

Wimpenny, S., Copley, A., & Ingleby, T. (2017). Fault mechanics and post-seismic deformation at Bam, SE Iran. *Geophysical Journal International*, *209*(2), 1018–1035.

Wright, T. J., Parsons, B. E., & Lu, Z. (2004). Toward mapping surface deformation in three dimensions using InSAR. *Geophysical Research Letters*, *31*(1). https://doi.org/10.1029/2003gl018827

Yin, A., Dang, Y.-Q., Wang, L.-C., Jiang, W.-M., Zhou, S.-P., Chen, X.-H., et al. (2008). Cenozoic tectonic evolution of Qaidam Basin and its surrounding regions (part 1): The southern Qilian Shan-Nan shan thrust belt and northern Qaidam Basin. *Geological Society of America Bulletin*, *120*(7–8), 813–846.

Yin, A., Dang, Y.-Q., Zhang, M., Chen, X.-H., & McRivette, M. W. (2008). Cenozoic tectonic evolution of the Qaidam Basin and its surrounding regions (part 3): Structural geology, sedimentation, and regional tectonic reconstruction. *Geological Society of America Bulletin*, *120*(7–8), 847–876.

Yonkee, A., & Weil, A. B. (2010). Reconstructing the kinematic evolution of curved mountain belts: Internal strain patterns in the Wyoming salient, Sevier thrust belt, USA. *GSA Bulletin*, *122*(1–2), 24–49.

Zhou, Y., Thomas, M. Y., Parsons, B., & Walker, R. T. (2018). Time-dependent postseismic slip following the 1978 Mw 7.3 Tabas-e-Golshan, Iran earthquake revealed by over 20 years of ESA InSAR observations. *Earth and Planetary Science Letters*, *483*, 64–75.

21699356, 2021, 3, Downloaded from https://agupubs.onlinelibrary.wiley.com/doi/10.1029/2020JB021241 by Cochrane France, Wiley Online Library on [10/03/2024]. See the Terms and Conditions (https://onlinelibrary.wiley.com/terms-and-conditions) on Wiley Online Library for rules of use; OA articles are governed by the applicable Creative Commons License